


## Article

# The Potential Effect on the Performance of CrN/Cr-Coated SS316L Bipolar Plates and Their Durability in Simulated Cathodic HT-PEFC Environments

Ruiyu Li <sup>1,2</sup>, Yun Cai <sup>1,2,\*</sup>, Yilin Liu <sup>1</sup>, Ziqi Xie <sup>1</sup>, Klaus Wippermann <sup>3</sup> and Werner Lehnert <sup>2,3</sup> 

<sup>1</sup> DeepHytec Co., Ltd., Shenzhen 518118, China; liruiyu@deephytec.com (R.L.); liuyilin@deephytec.com (Y.L.); xieziqi@deephytec.com (Z.X.)

<sup>2</sup> Faculty of Mechanical Engineering, RWTH Aachen University, 52072 Aachen, Germany; werner.lehnert@rwth-aachen.de

<sup>3</sup> Institute of Energy and Climate Research (IEK-14), Forschungszentrum Jülich GmbH, 52425 Jülich, Germany; k.wippermann@fz-juelich.de

\* Correspondence: caiyun\_wish@outlook.com

**Abstract:** This study further investigates the effect of potential on the corrosion resistance, the self-healing performance and the durability of CrN/Cr-coated SS316L bipolar plates with artificial defects (CR-316) in simulated cathodic HT-PEFC environments by means of electrochemical methods. The self-healing ability initiated by oxygen is relatively weak and needs the assistance of the cathode working potential for sealing. In some cases, the defects have spread over large parts of the bipolar plate. The influence of the potential on the corrosion resistance of the bare 316L and CR-316 specimens in the simulated cathodic HT-PEFC environments were investigated by electrochemical impedance spectroscopy. Moreover, the durability of the CR-316 specimens was examined under the various potential cycles in the simulated cathodic environment of HT-PEFC and O<sub>2</sub> atmosphere. After 5000 CV cycles in the potential range of 0.4–1.0 V vs. RHE, the CR-316 specimens could maintain the integrity and good corrosion resistance against the hot phosphoric acid. The results demonstrate the superior performance of CR-316 and make it a prime candidate as a non-precious coating for metallic bipolar plates on the cathode side of HT-PEFCs.

**Keywords:** corrosion; resistance; HT-PEFC; coating



**Citation:** Li, R.; Cai, Y.; Liu, Y.; Xie, Z.; Wippermann, K.; Lehnert, W. The Potential Effect on the Performance of CrN/Cr-Coated SS316L Bipolar Plates and Their Durability in Simulated Cathodic HT-PEFC Environments. *Energies* **2023**, *16*, 7528. <http://doi.org/10.3390/en16227528>

Academic Editor: Vladislav A. Sadykov

Received: 11 September 2023  
Revised: 28 October 2023  
Accepted: 1 November 2023  
Published: 11 November 2023



**Copyright:** © 2023 by the authors. Licensee MDPI, Basel, Switzerland. This article is an open access article distributed under the terms and conditions of the Creative Commons Attribution (CC BY) license (<https://creativecommons.org/licenses/by/4.0/>).

## 1. Introduction

Nowadays, electricity is vital to modern life. However, the most common way to obtain electricity is from burning fossil fuels like coal, gas, oil, etc., which are inefficient, non-renewable and environmentally unfriendly. Among a series of new technologies, people consider the hydrogen-fueled proton exchange membrane fuel cells (PEMFCs) to be a powerful potential approach for energy conversion due to their high energy density, zero-emissions, quiet operation and their use for various applications [1].

PEMFCs can be divided into two categories according to their working temperature. Low-temperature PEMFCs (LT-PEMFCs) commonly operate at temperatures below 100 °C. [2]. Moreover, only pure hydrogen can be used as a fuel. At present, hydrogen is still mainly produced by the steam reforming of gas and fossil fuels with inevitable impurities, such as CO [3–5]. Also, the massive storage technologies of pure hydrogen are not yet mature. Obviously, the pure hydrogen production cost is one of the main challenges in the LT-PEMFCs, where the existence of CO would cause serious poisoning of the catalysts [6].

An optional technology is the operation of PEMFCs at high temperatures. Compared to LT-PEMFCs, the following reasons make HT-PEMFCs commercially more attractive: Under high-temperature operation, there is no formation of liquid water and thus no requirement for a water management system. As the temperature increases, the reaction

kinetics become faster. Moreover, at temperatures above 140 °C, the CO tolerance increases significantly [7]. Therefore, hydrogen produced by steam reforming is suitable for HT-PEMFCs, thus lowering the production costs. Additionally, the cooling system can be simplified [8]. With these advantages, HT-PEMFCs have drawn a lot of attention from scientists and engineers all over the world [9–16].

The bipolar plate is fundamental to the performance of PEMFCs, especially power density [17]. A thickness of >2~5 mm of graphite-based BBPs is needed, which dramatically decreases the power density of the fuel cell [18]. Generally, graphite-based bipolar plates are produced by expensive computer numerical control (CNC) milling processes, which raises the cost [19]. Moreover, the poor mechanical properties limit the mass production of graphite-based BBPs [20]. For this reason, graphite-based BBPs are mainly used in stationary applications and for research purposes, where weight, volume and costs are not vital parameters [15].

In recent years, metallic BBPs have become the most attractive way to build PEMFC stacks owing to their good mechanical properties, low cost of mass production and reasonable electrical conductivity [21]. Various metals and metallic alloys have been investigated in making BBP substrates [20,22,23]. However, most studies have focused on stainless steel. Stainless steel (SS) can be a promising candidate for metallic BBPs because it is easy accessible and has good electrochemical properties [18]. Unfortunately, the harsh acidic and humid operating conditions of PEMFCs would easily attack metallic bipolar materials, leading to the release of metal cations and the formation of a passive oxide layer. Additionally, the increased interfacial contact resistance causes an additional voltage loss. A possible solution is an appropriate coating of the metallic BBPs to ensure both sufficient corrosion resistance and conductivity [24].

Significant studies have focused on coatings on metallic BBPs in LT-PEMFCs [25–34]. Due to the extremely harsh environments of HT-PEMFCs, most of the coatings that withstand LT-PEMFC conditions are ineffective in HT-PEMFCs. In a previous study, the influence of oxygen on the stability of the passivation layer (a type of a Cr-rich layer) formed on bare SS316L in hot phosphoric acid was investigated [35]. Then, a bi-layer chromium nitride/chromium (CrN/Cr) coating for HT-PEMFC application was designed, whose corrosion rates and interfacial contact resistance (ICR) in the simulated HT-PEMFC environments (85 wt.% H<sub>3</sub>PO<sub>4</sub> at RT and 130 °C) met the requirements of the U.S. Department of Energy (DOE) [36]. In particular, the CrN/Cr coating showed a self-healing ability initiated by oxygen in simulated cathodic HT-PEMFC environments when defects appeared on the surface of the coating [37].

As is known, the potential of fuel cell electrodes depends on the operation conditions. The constant variety of working potential will have a powerful influence on the properties of metallic bipolar plates. Therefore, it is important to investigate the influence of potential on the anti-corrosion performance of bipolar plates and its durability in the simulated HT-PEMFC environments. CrN/Cr-coated SS316L bipolar plates with artificial defects (CR-316) were chosen as the test objects of this study because they allow the electrochemical performance of CrN/Cr coatings to be checked at different locations (places with or without defects) by advanced impedance analysis. Uncoated (bare) SS316L specimens were used as the reference group. This study investigated the effect of the cathode potential on the self-healing performance, corrosion resistance and durability of CrN/Cr-coated and bare SS316L alloys in simulated cathodic HT-PEFC environments. It provides a way to extend the durability of the coating without the need for component replacement, and is expected to play a role in the practical application of fuel cell stacks.

## 2. Experimental Details

A special three-electrode cell that allows operation at temperatures higher than 100 °C was used in this study [14,38]. In brief, 85 wt.% H<sub>3</sub>PO<sub>4</sub> was used as the electrolyte, which was purchased from VWR Chemicals (Radnor, PA, USA) (AnalaR NORMAPUR); the specimen served as the working electrode (WE), while a reversible hydrogen electrode RHE

(HydroFlex, Gaskatel GmbH, Kassel, Germany) was employed as the reference electrode (RE) and a platinum mesh was used as the counter electrode (CE) [35]. Characterization of the SS316L samples by EDX has been carried out in a previous study [35]. The samples conformed to the characteristics of the nameplate and were from the same batch. The SS316L with a 0.1 mm thickness were chosen as the substrates in this study, using a closed-field unbalanced magnetron sputtering system with a background vacuum level of  $10^{-4}$  Pa. The stainless steel substrate was polished with sandpaper with a particle size of 1400, 1200, and 600, and the surface was cleaned with acetone before rapid drying. After the substrate was placed in the coating equipment, argon gas was introduced, and a Cr layer was first deposited at 200 °C, followed by an appropriate amount of nitrogen gas to assist in depositing a CrN layer by means of PVD (Teer Coating Ltd., Droitwich, UK) [37].

All measurements were performed with 85 wt.%  $\text{H}_3\text{PO}_4$  as the electrolyte at 130 °C in order to simulate the HT-PEFC environments. Electrochemical impedance spectroscopy (EIS) measurements were performed either under OCV (open circuit voltage) conditions or specific potentials in the range of 0.4–1.0 V (vs. RHE). The EIS data were then simulated by the THALES software (ZAHNER-Elektrik, Kronach, Germany). For a durability test, 5000 cycles of CV measurements were conducted in the potential range of 0.4–1.0 V vs. RHE with a scan rate of  $500 \text{ mV s}^{-1}$ . The chosen potential range corresponds to that of an HT-PEFC under varying operation conditions [39]. EIS spectra used for evaluating the stability of the CR-316 over the course of the durability test were recorded every 1000 cycles under OCV conditions, as soon as the free corrosion potential reached a stable value.

The surface morphologies of the CrN/Cr-SS316L before and after the 5000 CV cycles durability corrosion tests were investigated under high magnification using a Zeiss Gemini Ultra Plus scanning electron microscope (SEM) (Jena, Germany).

### 3. Results and Discussion

**Potential assistant self-healing ability.** The self-healing ability of the CR-316 specimens initiated by oxygen in simulated HT-PEFC environments has been validated in a previous study [29]. When the CR-316 specimens were actively damaged by applying a potential of 0.05 V under an  $\text{N}_2$  atmosphere until the corrosion current density reached  $1 \mu\text{A cm}^{-2}$  (case A), the damaged areas could be sealed by introducing oxygen into the electrolyte, as shown in Figure 1a. In contrast, when the CR-316 specimens were damaged more seriously by reaching a higher corrosion current density under the same operation, for example,  $3 \mu\text{A cm}^{-2}$  (case B), the increase in the free corrosion potential was very slow and the increment was small when purging the electrolyte with  $\text{O}_2$  at stage II (case B), as shown in Figure 1b. The potential stabilized at ca. 0.05 V in case B, which was much smaller than that of case A (ca. 0.35 V). However, after polarization at 0.65 V for 10 min, the free corrosion potential of the specimens stabilized at around 0.35 V again after removing the applied potential, as shown in red color for better visibility at stage IV in Figure 1b. This phenomenon indicates that the self-healing ability of the CR-316 specimens initiated by oxygen is moderate and can only be used for minor damages (e.g., case A). In the case of more serious damage (case B), the self-healing ability initiated by oxygen does not work properly and needs the assistance of the working potential of the HT-PEFC cathode, which is usually around 0.65 V. The free corrosion potential of case B with oxygen is 0.05 V, while the free corrosion potential of case B becomes higher after the assistance of polarization at 0.65 V for 10 min. The higher the free corrosion potential, the larger is the corresponding corrosion resistance. The increase in the free corrosion potential is attributed to the self-healing ability. According to Figure 2, the impedance at low frequencies of  $\text{N}_2$  purged and  $\text{O}_2$  purged samples were almost identical. However, when combining oxygen purging and a potential in the passive region, the low frequency impedance increased by one order of magnitude. This means that the corrosion resistance can be significantly improved with the assistance of potential and oxygen.

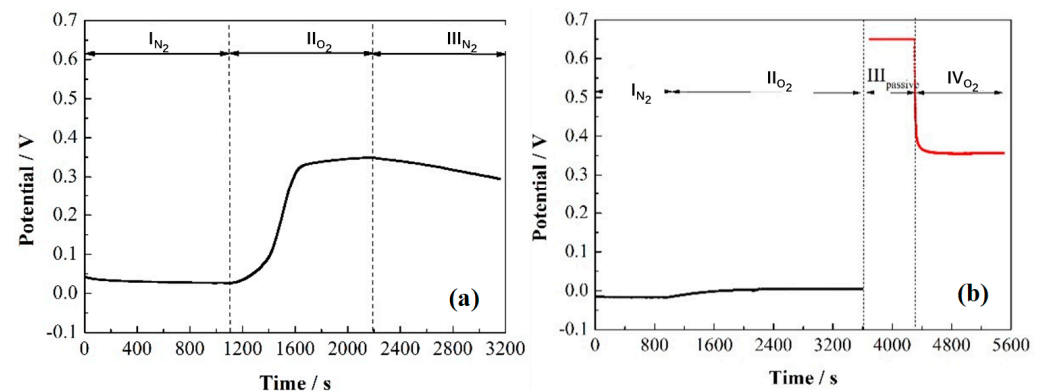


**Figure 1.** The healing process of the CR-316 specimens with defects under different conditions: (a) the self-healing process initiated by oxygen [37]; (b) the potential assistant self-healing process.

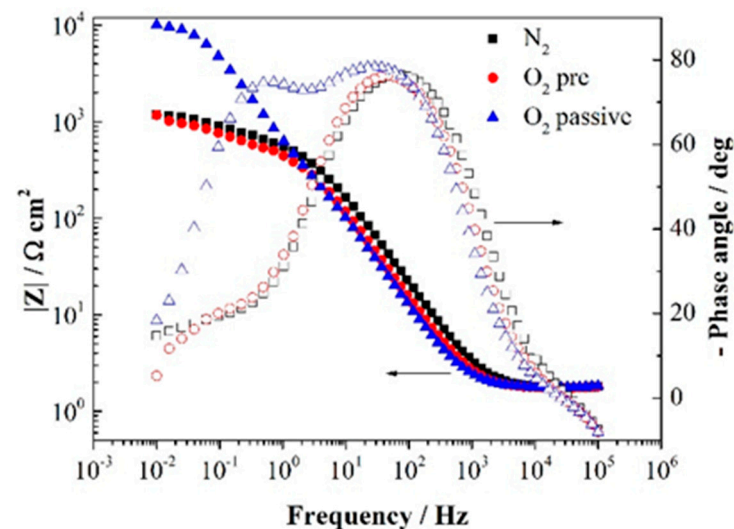


**Figure 2.** EIS spectra for CR-316 under OCV conditions in stages I, II and IV of Figure 1b.

A detailed analysis of the self-healing mechanism was carried out by EIS. The EIS spectra recorded at different stages are shown in Figure 2. The related equivalent circuits (ECs) used for the fitting of the spectra are presented in Figure 3a,b and the related simulated parameters are displayed in Table 1.  $R_s$  represents the resistance of the electrolyte,  $R_{pore}$  and  $C_{pore}$  describe the electrochemical behavior of a coating or a passive layer with defects, while the charge transfer resistance and double-layer capacitance ( $R_{ct}$  and  $C_{dl}$ ) depict the behavior of the substrate at the defects. As the charge transfer resistance is associated with corrosion processes,  $R_{ct}$  may also be considered as corrosion resistance. For the EIS data recorded prior to the onset of the potential assistant self-healing process, EC (c) including two time constants and an additional Warburg impedance is the most appropriate. The Warburg impedance represents a mass-transfer-dominated process in pitting corrosion. Attempts of fitting the above-mentioned impedance data without Warburg impedance were unsuccessful and resulted in large fitting errors. Figure 2 shows that the Bode plots of the CR-316 specimens recorded during stage I and II of case B (Figure 1b) were almost identical, except for the low-frequency area. The Warburg impedance in stage II was approximately three times smaller compared to that of stage I. It is assumed that the Warburg impedance represents the diffusion of corrosion products, e.g., metal ions, which is caused by localized corrosion at the defects in the CrN/Cr protection layer [37]. Thus, the Warburg impedance is associated with localized corrosion. For this reason, the decrease in the W-R value at stage II compared with that at stage I indicates that the presence of oxygen decreases the localized corrosion to some extent. However, the slight increment in corrosion potential

during phase II suggests that oxygen merely initiates a small self-healing effect in the case of a seriously damaged CrN/Cr coating (case B). The slight decrease in  $R_{ct}$  and  $R_{pore}$  at stage II compared with the values at stage I indicate that the degradation of the coatings continues at sites with and without defects.

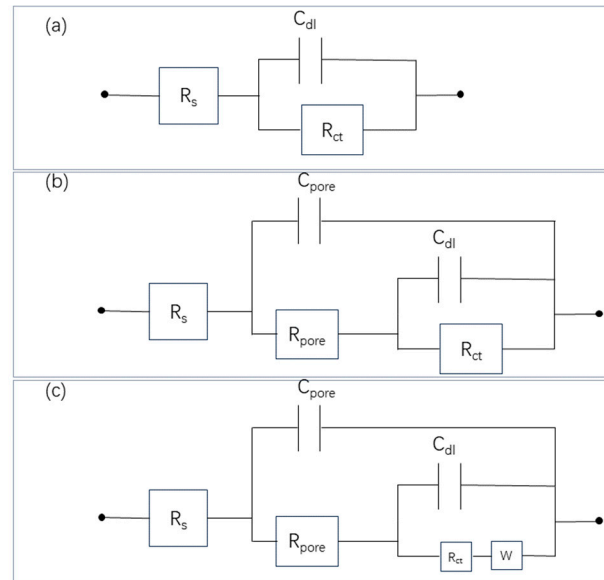


**Figure 3.** Equivalent circuits (EC) for the fitting of EIS spectra: (a) one time constant; (b) two time constants; (c) two time constants with a Warburg element.

**Table 1.** Fit results of EIS spectra of CR-316 shown in Figure 2.

Stage	$R_s$ ( $\Omega \text{ cm}^2$ )	$C_{dl}$ ( $\Omega^{-1} \text{ cm}^{-2} \text{ s}^{-n}$ )	$n_{dl}$	$R_{ct}$ ( $\Omega \text{ cm}^2$ )	$C_{pore}$ ( $\Omega^{-1} \text{ cm}^{-2} \text{ s}^{-n}$ )	$n_{pore}$	$R_{pore}$ ( $\Omega \text{ cm}^2$ )	W-R ( $\Omega \text{ cm}^2$ )
I-N <sub>2</sub>	1.78	$1.75 \times 10^{-3}$	0.63	$7.93 \times 10^2$	$1.26 \times 10^{-4}$	0.92	$5.63 \times 10^2$	16.84
II-O <sub>2</sub>	1.77	$2.26 \times 10^{-3}$	0.72	$5.54 \times 10^2$	$1.81 \times 10^{-4}$	0.92	$4.96 \times 10^2$	6.21
IV-O <sub>2</sub>	1.79	$1.08 \times 10^{-4}$	0.87	$1.16 \times 10^4$	$2.03 \times 10^{-4}$	0.93	$7.05 \times 10^2$	/

After passivation at 0.65 V (the normal working potential of the HT-PEFC cathode) for ca. 10 min, the Warburg impedance disappeared and, after removing the applied potential, the corrosion resistance increased by approximately one order of magnitude (comparative low-frequency impedance is included in Figure 2). As is shown in Table 1, it is the tenfold increase in the corrosion resistance,  $R_{ct}$ , that is responsible for the observed increase in the low-frequency resistance. Together with the corresponding disappearance of the Warburg impedance, this indicates that localized corrosion no longer takes place and the damaged areas are sealed after passivation under 0.65 V. Obviously, both small and large defects are sealed under these conditions, as is schematically shown in Figure 4c.

Potential effect on the corrosion resistance. From the anodic polarization of bare SS316L in simulated HT-PEFC environments, it has been shown that the passive region of this alloy lies within a potential range of 0.4–0.8 V [40,41]. At higher potentials, the anodic current steeply increases, indicating severe corrosion in the transpassive region. Figure 5 shows the EIS spectra of the bare and CR-316 specimens as a function of the applied potential in a simulated cathodic HT-PEFC environment. For bare SS316L, only one time constant (corresponding to one semi-arc in the Nyquist plot) was observed within the whole potential range, regardless of whether the electrolyte was purged by N<sub>2</sub> or O<sub>2</sub>. Therefore, the EIS spectra could be simulated by using the EC in Figure 3a, and the related fit values are shown in Table 2. The occurrence of only one time constant indicates that the bare surface was fully covered with a stable oxide film. When comparing the EI spectra



in Figure 5a,b, and the related simulated values in Table 2, the electrochemical properties of the passive layers formed under  $N_2$  and  $O_2$  atmospheres turn out to be quite similar. For both  $N_2$  and  $O_2$  atmospheres, the total resistance of the impedance, which is almost identical to  $R_{ct}$ , increases with the applied DC potential and reaches a maximum at around 0.6 V. At higher potentials, it starts to decrease in both  $N_2$ - and  $O_2$ -purging atmospheres.

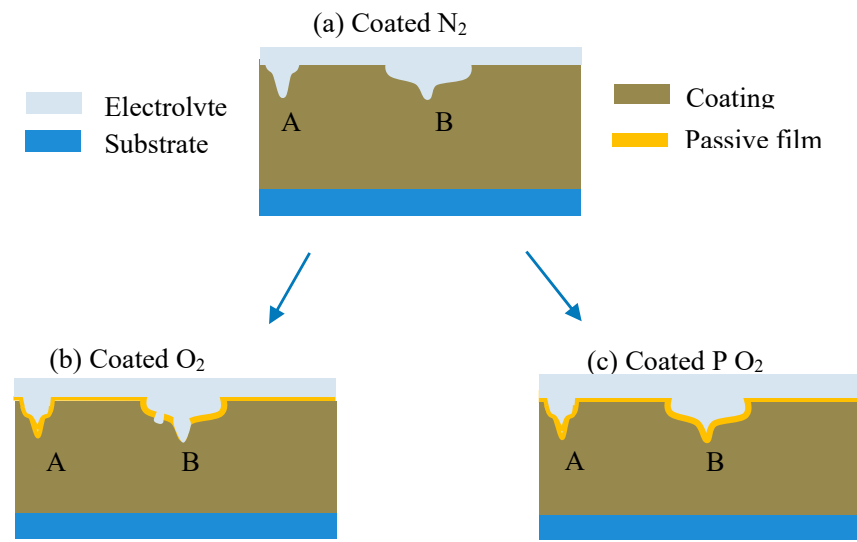


**Figure 4.** Schematic representation of the interface CR-316/85 wt.%  $H_3PO_4$  at 130 °C: (a) CR-316 with small defect (A) and large defect (B) under  $N_2$ -purging atmosphere; (b) CR-316 with small defect (A) and large defect (B) under  $O_2$ -purging atmosphere; (c) CR-316 with small defect (A) and large defect (B) under  $O_2$ -purging atmosphere after polarization.

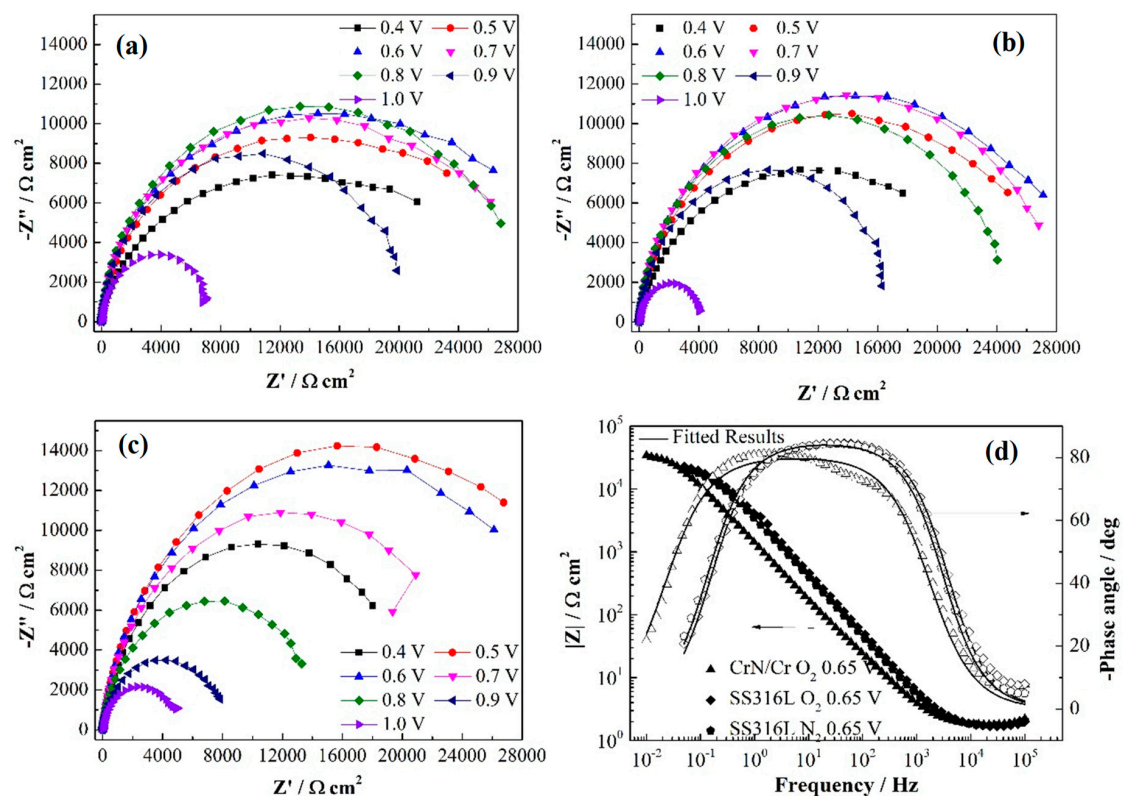


**Figure 5.** EIS spectra of bare and CrN/Cr-coated SS316L as a function of potential: (a) Nyquist plots of bare SS316L,  $N_2$ ; (b) Nyquist plots of bare SS316L,  $O_2$ ; (c) Nyquist plots of CrN/Cr-coated SS316L,  $O_2$ ; (d) Bode plots of both bare and CrN/Cr-coated SS316L, 0.65 V.

**Table 2.** Fit results of EIS spectra of bare SS316L shown in Figure 5a,b.

Sample	$R_s$ ( $\Omega \text{ cm}^2$ )	$C_{dl}$ ( $\Omega^{-1} \text{ cm}^{-2} \text{ s}^{-n}$ )	$n_{dl}$	$R_{ct}$ ( $\Omega \text{ cm}^2$ )	Sample	$R_s$ ( $\Omega \text{ cm}^2$ )	$C_{dl}$ ( $\Omega^{-1} \text{ cm}^{-2} \text{ s}^{-n}$ )	$n_{dl}$	$R_{ct}$ ( $\Omega \text{ cm}^2$ )
N <sub>2</sub> -0.4	1.67	$7.82 \times 10^{-5}$	0.88	$1.92 \times 10^4$	O <sub>2</sub> -0.4	1.60	$7.83 \times 10^{-5}$	0.89	$1.88 \times 10^4$
N <sub>2</sub> -0.5	1.69	$5.67 \times 10^{-5}$	0.91	$2.26 \times 10^4$	O <sub>2</sub> -0.5	1.63	$5.50 \times 10^{-5}$	0.91	$2.46 \times 10^4$
N <sub>2</sub> -0.6	1.67	$4.81 \times 10^{-5}$	0.91	$2.53 \times 10^4$	O <sub>2</sub> -0.6	1.63	$4.67 \times 10^{-5}$	0.92	$2.67 \times 10^4$
N <sub>2</sub> -0.7	1.69	$4.20 \times 10^{-5}$	0.92	$2.46 \times 10^4$	O <sub>2</sub> -0.7	1.62	$4.15 \times 10^{-5}$	0.93	$2.61 \times 10^4$
N <sub>2</sub> -0.8	1.71	$3.74 \times 10^{-5}$	0.92	$2.60 \times 10^4$	O <sub>2</sub> -0.8	1.63	$3.77 \times 10^{-5}$	0.93	$2.37 \times 10^4$
N <sub>2</sub> -0.9	1.69	$3.72 \times 10^{-5}$	0.93	$1.99 \times 10^4$	O <sub>2</sub> -0.9	1.61	$3.81 \times 10^{-5}$	0.93	$1.74 \times 10^4$
N <sub>2</sub> -1.0	1.63	$5.81 \times 10^{-5}$	0.92	$7.9 \times 10^3$	O <sub>2</sub> -1.0	1.55	$9.02 \times 10^{-5}$	0.92	$4.43 \times 10^3$

As with the CR-316 samples, the EIS spectra of CrN/Cr-coated SS316L show two time constants without Warburg impedance, as shown in Figure 5c,d. This applies to the whole potential range investigated. Therefore, the EIS spectra of the CR-316 specimens were fitted by using the EC in Figure 3b. Table 3 shows the fit results of the Nyquist plots of CrN/Cr-coated SS316L, whereas Table 4 refers to the Bode plots of both bare and CrN/Cr-coated SS316L. The corrosion resistance of the coating ( $R_{ct}$ ) shows a similar trend compared with the passive film formed on the surface of bare SS316L. This is reasonable because the passive layer formed on the surface of a bare SS316L specimen in the simulated cathodic HT-PEFC environment is also a type of a Cr-rich layer. This finding indicates that the corrosion resistance of the CrN/Cr coating is highly influenced by potential-induced passivation. Another interesting effect is that the corrosion resistance of the coating via the defects ( $R_{pore}$ ) shows a trend of continuously decreasing with increasing applied potential. The decreasing  $R_{pore}$  under passivation conditions indicates increasing local corrosion at the defects. When increasing the potential from 0.65 to 1.0 V, the corrosion resistance of the bare and CrN/Cr-coated SS316L specimens decreases by approximately 80%. The same trend for both CrN/Cr-coated and uncoated SS316L can be explained by the fact that their passivation layers are both Cr-rich. The similar behavior of coated and uncoated SS316L in the passive region might suggest that the coating may be unnecessary. However, this is not the case. CrN/Cr-coated SS316L has clear advantages compared to the bare alloy: (i) without applying a (passive) potential, the coating is much more stable; (ii) the interfacial resistance of the CrN/Cr coating and thus the bipolar plate with the MEA is significantly reduced; (iii) in terms of corrosion, only Cr ions are released, whereas several metal ions are released in the case of the bare alloy; and (iv) the durability of the coated sample is orders of magnitude higher than that of the bare alloy (see durability section).

**Table 3.** Fit results of EIS spectra of CrN/Cr-coated SS316L shown in Figure 5c.

Stage	$R_s$ ( $\Omega \text{ cm}^2$ )	$C_{dl}$ ( $\Omega^{-1} \text{ cm}^{-2} \text{ s}^{-n}$ )	$n_{dl}$	$R_{ct}$ ( $\Omega \text{ cm}^2$ )	$C_{pore}$ ( $\Omega^{-1} \text{ cm}^{-2} \text{ s}^{-n}$ )	$n_{pore}$	$R_{pore}$ ( $\Omega \text{ cm}^2$ )
O <sub>2</sub> -0.4	1.76	$5.59 \times 10^{-5}$	0.95	$2.25 \times 10^4$	$1.28 \times 10^{-4}$	0.87	$3.24 \times 10^2$
O <sub>2</sub> -0.5	1.81	$2.68 \times 10^{-5}$	0.95	$3.39 \times 10^4$	$1.20 \times 10^{-4}$	0.89	$1.35 \times 10^2$
O <sub>2</sub> -0.6	1.80	$2.71 \times 10^{-5}$	0.96	$3.04 \times 10^4$	$1.32 \times 10^{-4}$	0.89	$1.13 \times 10^2$
O <sub>2</sub> -0.7	1.81	$2.52 \times 10^{-5}$	0.98	$2.54 \times 10^4$	$1.39 \times 10^{-4}$	0.89	70.08
O <sub>2</sub> -0.8	1.80	$2.76 \times 10^{-5}$	1.0	$1.50 \times 10^4$	$1.66 \times 10^{-4}$	0.88	57.58
O <sub>2</sub> -0.9	1.80	$2.92 \times 10^{-5}$	1.0	$8.34 \times 10^3$	$1.83 \times 10^{-4}$	0.86	48.97
O <sub>2</sub> -1.0	1.77	$4.64 \times 10^{-5}$	1.0	$5.30 \times 10^3$	$2.30 \times 10^{-4}$	0.83	47.83

**Durability.** In order to simulate the various working conditions, the influence of time and the electrode potential on the durability of CR-316 specimens was investigated. For this purpose, 5000 CV cycles with a scan rate of  $500 \text{ mV s}^{-1}$  were performed in the potential range of 0.4 to 1 V vs. RHE. Figure 6a shows the free corrosion current densities of the CR-316 specimen as a function of the number of cycles. It turns out that the free corrosion current densities remain stable within 5000 CV cycles in the simulated cathodic

environment of HT-PEFCs. The observed fluctuations in current density during the first 500 cycles can be explained by active dissolution and repassivation of the sample, before more or less stable conditions are achieved after 500 cycles (approximately 20 min). Figure 6b shows the EIS spectra of the CR-316 specimens as the function of the number of cycles. The EIS spectra were fitted by using the EC in Figure 3b, and the values are shown in Table 5.

**Table 4.** Fit results of EIS spectra of bare and CrN/Cr-coated SS316L shown in Figure 5d.

Stage	$R_s$ ( $\Omega \text{ cm}^2$ )	$C_{dl}$ ( $\Omega^{-1} \text{ cm}^{-2} \text{ s}^{-n}$ )	$n_{dl}$	$R_{ct}$ ( $\Omega \text{ cm}^2$ )	$C_{pore}$ ( $\Omega^{-1} \text{ cm}^{-2} \text{ s}^{-n}$ )	$n_{pore}$	$R_{pore}$ ( $\Omega \text{ cm}^2$ )
bare-N <sub>2</sub>	1.76	$5.11 \times 10^{-5}$	0.94	$2.29 \times 10^4$	/	/	/
bare-O <sub>2</sub>	1.70	$4.19 \times 10^{-5}$	0.95	$2.36 \times 10^4$	/	/	/
coated-O <sub>2</sub>	1.80	$3.23 \times 10^{-5}$	0.94	$2.88 \times 10^4$	$1.28 \times 10^{-4}$	0.89	69.01

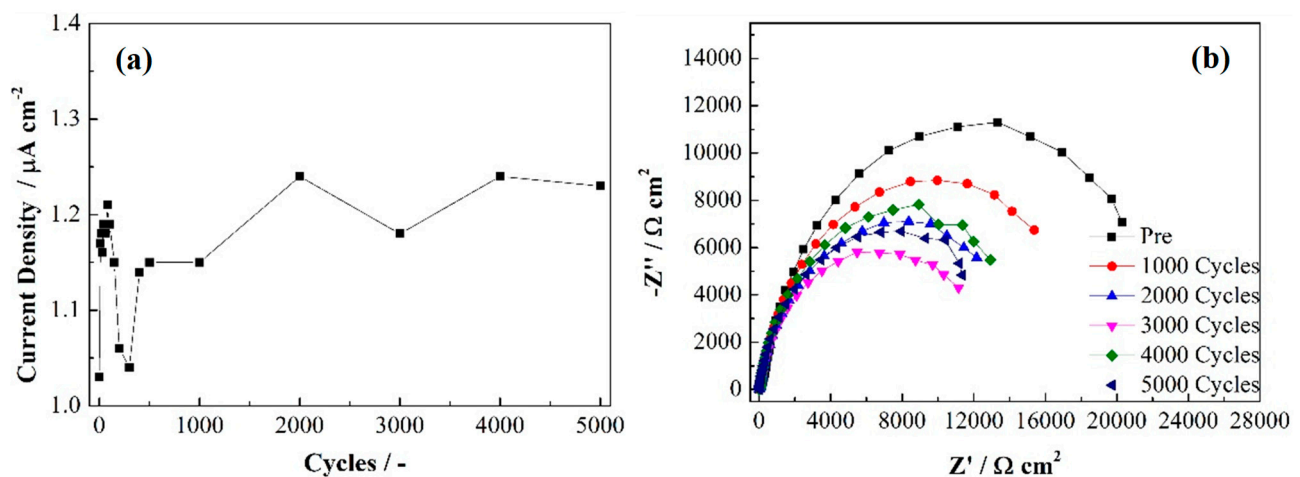


**Figure 6.** Durability performance of the CR-316 specimens with potential cycles: (a) free corrosion current density; (b) EIS.

**Table 5.** Fit results of EIS spectra of CR-316 shown in Figure 6b.

Stage	$R_s$ ( $\Omega \text{ cm}^2$ )	$C_{dl}$ ( $\Omega^{-1} \text{ cm}^{-2} \text{ s}^{-n}$ )	$n_{dl}$	$R_{ct}$ ( $\Omega \text{ cm}^2$ )	$C_{pore}$ ( $\Omega^{-1} \text{ cm}^{-2} \text{ s}^{-n}$ )	$n_{pore}$	$R_{pore}$ ( $\Omega \text{ cm}^2$ )
pre	1.80	$1.01 \times 10^{-4}$	0.9	$2.76 \times 10^4$	$6.72 \times 10^{-5}$	0.91	$6.17 \times 10^2$
1000	1.77	$1.56 \times 10^{-4}$	0.92	$2.17 \times 10^4$	$1.16 \times 10^{-4}$	0.87	$2.80 \times 10^2$
2000	1.76	$1.75 \times 10^{-4}$	0.92	$1.77 \times 10^4$	$1.45 \times 10^{-4}$	0.85	$1.83 \times 10^2$
3000	1.76	$1.81 \times 10^{-4}$	0.93	$1.41 \times 10^4$	$1.68 \times 10^{-4}$	0.84	$1.25 \times 10^2$
4000	1.78	$1.38 \times 10^{-4}$	0.93	$1.92 \times 10^4$	$1.69 \times 10^{-4}$	0.85	94.89
5000	1.77	$1.45 \times 10^{-4}$	0.93	$1.70 \times 10^4$	$1.95 \times 10^{-4}$	0.83	77.19

It was observed that the coating showed degradation in the first 3000 cycles, while maintaining stability after 3000 CV cycles in the simulated cathodic HT-PEFC environments. Moreover, the corrosion resistance ( $R_{ct}$ ) of the coating after 5000 CV cycles is hundreds of times higher than that of bare SS316L [29]. The corrosion current density of the CR-316 specimen was still ca.  $1 \mu\text{A cm}^{-2}$ . These results indicate that the influence of the continuously changing potential on the durability of the CrN/Cr-coated SS316L bipolar plates in the simulated cathodic HT-PEFC environments was very small. This suggests that CrN/Cr-coated SS316L bipolar plates are durable, even under the dynamic operation of an HT-PEMFC. This is particularly important for mobile applications such as use in cars or airplanes, where the bipolar plates and other components of the HT-PEMFC ought to withstand frequently changing currents.



The surface morphologies of the CR-316 specimens before and after 5000 CV cycles are shown in Figure 7. The surface of the CR-316L specimen after 5000 CV cycles shows no spalling of the coating (Figure 7b). This indicates that the CrN/Cr coating still maintains its integrity after 5000 CV cycles in the simulated cathodic HT-PEMFC environments. Therefore, the CrN/Cr-coated SS316L specimens with defects showed good durability performance in the simulated cathodic HT-PEMFC environments.

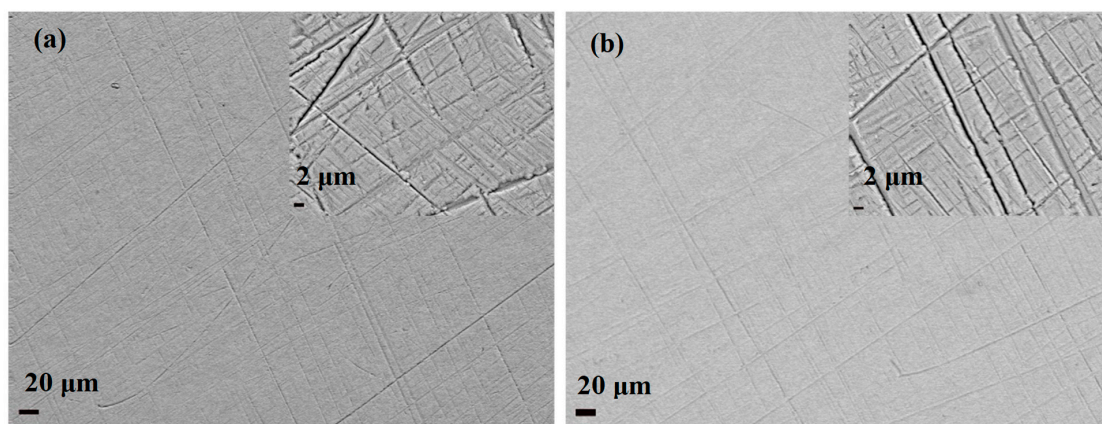


**Figure 7.** SEM of CrN/Cr-coated SS316L specimens before and after 5000 h durability tests: (a) fresh sample; (b) after 5000 CV cycles.

#### 4. Conclusions

This study demonstrated the potential assistant self-healing ability and durability of CrN/Cr-coated SS316L specimens with defects in simulated cathodic HT-PEFC environments. The self-healing ability initiated by oxygen is relatively weak and can be considerably enhanced by the cathode potential. By means of impedance spectroscopy, the effect of the electrode potential on the corrosion resistance of the CrN/Cr coatings and the passive layers on the surface of bare SS316L were analyzed in detail. It became apparent that the CrN/Cr-coated SS316L specimen remained intact, even after the dynamic operation of 5000 CV cycles and the harsh conditions of simulated cathodic HT-PEFC environments. This study suggests that CrN/Cr-coated SS316L bipolar plates have high durability in the cathodic environment of HT-PEFCs, and should be suitable for mobile applications of HT-PEFCs with frequently varying currents and potentials.

**Author Contributions:** Methodology, R.L.; Software, R.L. and Z.X.; Validation, Z.X.; Formal analysis, R.L.; Investigation, Y.L.; Data curation, Y.C.; Writing—original draft, R.L. and Y.C.; Writing—review & editing, K.W.; Visualization, Y.L.; Supervision, W.L. All authors have read and agreed to the published version of the manuscript.

**Funding:** This research received no external funding.

**Data Availability Statement:** Data are contained within the article.

**Acknowledgments:** We would like to express our thanks to Andreas Everwand for performing the SEM measurements.

**Conflicts of Interest:** Author Ruiyu Li, Yun Cai, Yilin Liu, and Ziqi Xie were employed by DeepHytec Co., Ltd. The remaining authors declare that the research was conducted in the absence of any commercial or financial relationships that could be construed as a potential conflict of interest.

#### References

- Haider, R.; Wen, Y.; Ma, Z.-F.; Wilkinson, D.P.; Zhang, L.; Yuan, X.; Song, S.; Zhang, J. High temperature proton exchange membrane fuel cells: Progress in advanced materials and key technologies. *Chem. Soc. Rev.* **2021**, *50*, 1138–1187. [[CrossRef](#)]
- Rosli, R.E.; Sulong, A.B.; Daud, W.R.W.; Zulkifley, M.A.; Husaini, T.; Rosli, M.I.; Majlan, E.H.; Haque, M.A. A review of high-temperature proton exchange membrane fuel cell (HT-PEMFC) system. *Int. J. Hydrogen Energy* **2017**, *42*, 9293–9314. [[CrossRef](#)]

3. Ni, M.; Leung, D.Y.C.; Leung, M.K.H. A review on reforming bio-ethanol for hydrogen production. *Int. J. Hydrogen Energy* **2007**, *32*, 3238–3247. [\[CrossRef\]](#)
4. Rostrup-Nielsen, J.R.; Sehested, J.; Nørskov, J.K. Hydrogen and synthesis gas by steam- and CO<sub>2</sub> reforming. *Adv. Catal.* **2002**, *47*, 65–139. [\[CrossRef\]](#)
5. Ito, H.; Maeda, T.; Nakano, A.; Takenaka, H. Properties of Nafion membranes under PEM water electrolysis conditions. *Int. J. Hydrogen Energy* **2011**, *36*, 10527–10540. [\[CrossRef\]](#)
6. Li, R. *Coatings for Metallic Bipolar Plates in High-Temperature Polymer Electrolyte Fuel Cells*; Forschungszentrum Jülich GmbH, Zentralbibliothek: Jülich, Germany, 2019; Volume 472.
7. Oh, K.; Ju, H. Temperature dependence of CO poisoning in high-temperature proton exchange membrane fuel cells with phosphoric acid-doped polybenzimidazole membranes. *Int. J. Hydrogen Energy* **2015**, *40*, 7743–7753. [\[CrossRef\]](#)
8. Barreras, F.; Lozano, A.; Roda, V.; Barroso, J.; Martín, J. Optimal design and operational tests of a high-temperature PEM fuel cell for a combined heat and power unit. *Int. J. Hydrogen Energy* **2014**, *39*, 5388–5398. [\[CrossRef\]](#)
9. Chandan, A.; Hattenberger, M.; El-Kharouf, A.; Du, S.; Dhir, A.; Self, V.; Pollet, B.G.; Ingram, A.; Bujalski, W. High temperature (HT) polymer electrolyte membrane fuel cells (PEMFC)—A review. *J. Power Sources* **2013**, *231*, 264–278. [\[CrossRef\]](#)
10. Pinar, F.J.; Pilinski, N.; Wagner, P. Long-term testing of a high temperature polymer electrolyte membrane fuel cell: The effect of reactant gases. *AIChE J.* **2016**, *62*, 217–227. [\[CrossRef\]](#)
11. Sharaf, O.Z.; Orhan, M.F. An overview of fuel cell technology: Fundamentals and applications. *Renew. Sustain. Energy Rev.* **2014**, *32*, 810–853. [\[CrossRef\]](#)
12. Authayanun, S.; Im-Orb, K.; Arpornwichanop, A. A review of the development of high temperature proton exchange membrane fuel cells. *Cuihua Xuebao/Chin. J. Catal.* **2015**, *36*, 473–483. [\[CrossRef\]](#)
13. Samsun, R.C.; Pasel, J.; Janßen, H.; Lehnert, W.; Peters, R.; Stolten, D. Design and test of a 5kWe high-temperature polymer electrolyte fuel cell system operated with diesel and kerosene. *Appl. Energy* **2014**, *114*, 238–249. [\[CrossRef\]](#)
14. Weissbecker, V.; Reimer, U.; Wippermann, K.; Lehnert, W. A Comprehensive Corrosion Study on Metallic Materials for HT-PEFC Application. *ECS Trans.* **2013**, *58*, 693–704. [\[CrossRef\]](#)
15. Manso, A.P.; Marzo, F.F.; Garicano, X.; Alegre, C.; Lozano, A.; Barreras, F. Corrosion behavior of tantalum coatings on AISI 316L stainless steel substrate for bipolar plates of PEM fuel cells. *Int. J. Hydrogen Energy* **2020**, *45*, 20679–20691. [\[CrossRef\]](#)
16. Alegre, C.; Álvarez-Manuel, L.; Mustata, R.; Valiño, L.; Lozano, A.; Barreras, F. Assessment of the durability of low-cost Al bipolar plates for High Temperature PEM fuel cells. *Int. J. Hydrogen Energy* **2019**, *44*, 12748–12759. [\[CrossRef\]](#)
17. Yang, L.X.; Liu, R.J.; Wang, Y.; Liu, H.J.; Zeng, C.L.; Fu, C. Corrosion and interfacial contact resistance of nanocrystalline  $\beta$ -Nb<sub>2</sub>N coating on 430 FSS bipolar plates in the simulated PEMFC anode environment. *Int. J. Hydrogen Energy* **2021**, *46*, 32206–32214. [\[CrossRef\]](#)
18. Ingle, A.V.; Raja, V.S.; Rangarajan, J.; Mishra, P. Corrosion resistant quaternary Al–Cr–Mo–N coating on type 316L stainless steel bipolar plates for proton exchange membrane fuel cells. *Int. J. Hydrogen Energy* **2020**, *45*, 3094–3107. [\[CrossRef\]](#)
19. Yan, W.M.; Chen, C.Y.; Liang, C.H. Comparison of performance degradation of high temperature PEM fuel cells with different bipolar plates. *Energy* **2019**, *186*, 115836. [\[CrossRef\]](#)
20. Gao, P.; Xie, Z.; Wu, X.; Ouyang, C.; Lei, T.; Yang, P.; Liu, C.; Wang, J.; Ouyang, T.; Huang, Q. Development of Ti bipolar plates with carbon/PTFE/TiN composites coating for PEMFCs. *Int. J. Hydrogen Energy* **2018**, *43*, 20947–20958. [\[CrossRef\]](#)
21. Jin, J.; Hu, M.; Zhao, X. Investigation of incorporating oxygen into TiN coating to resist high potential effects on PEMFC bipolar plates in vehicle applications. *Int. J. Hydrogen Energy* **2020**, *45*, 23310–23326. [\[CrossRef\]](#)
22. Silva, F.; Ramirez, O.P.; Tunes, M.; Edmondson, P.; Sagás, J.; Fontana, L.; de Melo, H.; Schön, C. Corrosion resistance of functionally graded TiN/Ti coatings for proton exchange membrane fuel cells. *Int. J. Hydrogen Energy* **2020**, *45*, 33993–34010. [\[CrossRef\]](#)
23. Lee, E.-K.; Kim, J.-K.; Kim, T.-J.; Song, H.; Kim, J.-H.; Park, S.-A.; Jeong, T.-G.; Yun, S.-W.; Lee, J.; Goo, J.; et al. Enhanced corrosion resistance and fuel cell performance of Al1050 bipolar plate coated with TiN/Ti double layer. *Energy Convers. Manag.* **2013**, *75*, 727–733. [\[CrossRef\]](#)
24. Peng, S.; Xu, J.; Li, Z.; Jiang, S.; Munroe, P.; Xie, Z.-H.; Lu, H. A reactive-sputter-deposited TiSiN nanocomposite coating for the protection of metallic bipolar plates in proton exchange membrane fuel cells. *Ceram. Int.* **2020**, *46*, 2743–2757. [\[CrossRef\]](#)
25. Feng, K.; Li, Z.; Sun, H.; Yu, L.; Cai, X.; Wu, Y.; Chu, P.K. C/CrN multilayer coating for polymer electrolyte membrane fuel cell metallic bipolar plates. *J. Power Sources* **2013**, *222*, 351–358. [\[CrossRef\]](#)
26. Zhang, M.; Lin, G.; Wu, B.; Shao, Z. Composition optimization of arc ion plated CrN x films on 316L stainless steel as bipolar plates for polymer electrolyte membrane fuel cells. *J. Power Sources* **2012**, *205*, 318–323. [\[CrossRef\]](#)
27. Zhang, H.; Lin, G.; Hou, M.; Hu, L.; Han, Z.; Fu, Y.; Shao, Z.; Yi, B. CrN/Cr multilayer coating on 316L stainless steel as bipolar plates for proton exchange membrane fuel cells. *J. Power Sources* **2012**, *198*, 176–181. [\[CrossRef\]](#)
28. Nam, N.D.; Kim, J.G. Electrochemical behavior of CrN coated on 316L stainless steel in simulated cathodic environment of proton exchange membrane fuel cell. *Jpn. J. Appl. Phys.* **2008**, *47*, 6887–6890. [\[CrossRef\]](#)
29. Mori, Y.; Ueda, M.; Hashimoto, M.; Aoi, Y.; Tanase, S.; Sakai, T. Amorphous carbon coated stainless separator for PEFCs. *Surf. Coat. Technol.* **2008**, *202*, 4094–4101. [\[CrossRef\]](#)
30. Yi, P.; Zhang, D.; Qiu, D.; Peng, L.; Lai, X. Carbon-based coatings for metallic bipolar plates used in proton exchange membrane fuel cells. *Int. J. Hydrogen Energy* **2019**, *44*, 6813–6843. [\[CrossRef\]](#)

31. Bi, J.; Yang, J.; Liu, X.; Wang, D.; Yang, Z.; Liu, G.; Wang, X. Development and evaluation of nitride coated titanium bipolar plates for PEM fuel cells. *Int. J. Hydrogen Energy* **2021**, *46*, 1144–1154. [[CrossRef](#)]
32. Chanda, U.K.; Padhee, S.P.; Pandey, A.K.; Roy, S.; Pati, S. Electrodeposited Ni–Mo–Cr–P coatings for AISI 1020 steel bipolar plates. *Int. J. Hydrogen Energy* **2020**, *45*, 21892–21904. [[CrossRef](#)]
33. Agarwal, H.; Pandey, R.; Bhat, S.D. Improved polymer electrolyte fuel cell performance with membrane electrode assemblies using modified metallic plate: Comparative study on impact of various coatings. *Int. J. Hydrogen Energy* **2020**, *45*, 18731–18742. [[CrossRef](#)]
34. Haye, E.; Deschamps, F.; Caldarella, G.; Piedboeuf, M.-L.; Lafort, A.; Cornil, H.; Colomer, J.-F.; Pireaux, J.-J.; Job, N. Formable chromium nitride coatings for proton exchange membrane fuel cell stainless steel bipolar plates. *Int. J. Hydrogen Energy* **2020**, *45*, 15358–15365. [[CrossRef](#)]
35. Li, R.; Cai, Y.; Wippermann, K.; Lehnert, W. Corrosion and Electrical Properties of SS316L Materials in the Simulated HT-PEFC Environment. *J. Electrochem. Soc.* **2018**, *165*, C681–C688. [[CrossRef](#)]
36. Janßen, H.; Edelmann, A.; Mildebrath, T.; Müller, P.; Lehnert, W.; Stolten, D. Design and experimental validation of an HT-PEFC stack with metallic BPP. *Int. J. Hydrogen Energy* **2018**, *43*, 18488–18497. [[CrossRef](#)]
37. Li, R.; Cai, Y.; Wippermann, K.; Lehnert, W. The Electrochemical Behavior of CrN/Cr Coatings with Defects on 316L Stainless Steel in the Simulated Cathodic Environment of an HT-PEFC. *J. Electrochem. Soc.* **2019**, *166*, C394–C400. [[CrossRef](#)]
38. Weissbecker, V.; Wippermann, K.; Lehnert, W. Electrochemical Corrosion Study of Metallic Materials in Phosphoric Acid as Bipolar Plates for HT-PEFCs. *J. Electrochem. Soc.* **2014**, *161*, F1437–F1447. [[CrossRef](#)]
39. Kaserer, S.; Rakousky, C.; Melke, J.; Roth, C. Design of a Reference Electrode for High-Temperature PEM Fuel Cells. *J. Appl. Electrochem.* **2013**, *43*, 1069–1078. [[CrossRef](#)]
40. Li, R.; Cai, Y.; Reimer, U.; Wippermann, K.; Shao, Z.; Lehnert, W. CrN/Cr-Coated Steel Plates for High-Temperature Polymer Electrolyte Fuel Cells: Performance and Durability. *J. Electrochem. Soc.* **2020**, *167*, 144507. [[CrossRef](#)]
41. RLi YCai KWippermann, W. Lehnert, Bilayer CrN/Cr coating-modified 316L stainless steel bipolar plates for high temperature polymer electrolyte fuel cells. *J. Power Sources* **2019**, *434*, 226718. [[CrossRef](#)]

**Disclaimer/Publisher’s Note:** The statements, opinions and data contained in all publications are solely those of the individual author(s) and contributor(s) and not of MDPI and/or the editor(s). MDPI and/or the editor(s) disclaim responsibility for any injury to people or property resulting from any ideas, methods, instructions or products referred to in the content.